

# Optical QPOs with dual periodicities 1103days and 243days in the blue quasar SDSS J100438.8+151056

GuiLin Liao<sup>1</sup>, XingQian Chen<sup>1</sup>, Qi Zheng<sup>1</sup>, YiLin Liu<sup>1</sup>, and XueGuang Zhang<sup>1,\*</sup>

School of Physical Science and Technology, GuangXi University, No.100, Daxue East Road, Nanning, 530004, P. R. China

## ABSTRACT

This manuscript investigates the possible existence of a binary supermassive black holes (BSMBH) system in the blue quasar SDSS J100438.8+151056 (=SDSS J1004+1510) at  $z=0.219$  based on the detection of robust optical QPOs. We determine QPOs using multiple analysis methods applied to the CSS-V, ZTF g/r band light curves, and additionally, combined with the characteristics of broad emission lines and explores potential mechanisms for the QPOs, including jet and disk precession models. Two distinct periodicities,  $1103 \pm 260$ days and  $243 \pm 29$ days, are identified in the ZTF g/r-band light curves with confidence level exceeding  $5\sigma$ , through four different techniques. Meanwhile, the  $1103 \pm 260$ days periodicity is also clearly detected in the CSS V-band light curve. The optical periodicities suggest a BSMBH system candidate in SDSS J1004+1510, with an estimated total virial BH mass of  $(1.13 \pm 0.14) \times 10^8 M_\odot$  and a space separation of  $0.0053 \pm 0.0016$ pc for the periodicity of  $1103 \pm 260$ days. The second periodicity of  $243 \pm 29$ days could be attributed to harmonic oscillations, considering  $(1103 \pm 260)/(243 \pm 29) \sim 4.54 \pm 0.47$  with large scatters. However, if the periodicity of  $243 \pm 29$ days was from an independent QPO, a triple BH system candidate on sub-pc scale could be probably expected, with space separations of  $0.00036 \pm 0.00004$ pc between a close BSMBH system and of  $0.0053 \pm 0.0016$ pc between the BSMBH system and the third BH, after considering similar BH mass of the third BH as the total mass of the central BSMBH. These findings strongly demonstrate that combined light curves from the different sky survey projects can lead to more reliable QPOs candidates to be detected, and also indicate higher quality light curves could be helpful to find probably potential QPOs with multiple periodicities leading to rare detections of candidates for sub-pc triple BH systems.

**Key words.** galaxies:active - galaxies:nuclei - quasars:emission lines - quasars: individual (SDSS J1004+1510)

## 1. Introduction

Galaxy merging is an important part of the formation and evolution of galaxies in the universe (Carlberg 1992; Kauffmann, White & Guiderdoni 1993; Lacey & Cole 1994; Barnes & Hernquist 1996; Silk & Rees 1998; Menou, Haiman & Narayanan 2001; Lin et al. 2004; Bundy et al. 2009; Merritt 2006; Satyapal et al. 2014; Rodriguez et al. 2016, 2017; Bottrell et al. 2019; Martin et al. 2021; Jackson et al. 2021; Yoon et al. 2022; Lokas 2023; Kim et al. 2024). Almost every galaxy has a BH at its center (Kormendy & Richstone 1995; Ferrarese & Ford 2005; Kormendy & Ho 2013; Heckman & Best 2014). It means that the process of galaxy mergers is often accompanied by the formation of dual Active Galactic Nuclei (dual AGN) on kpc scale and binary supermassive black holes (BSMBH) systems on sub-pc scale (Begelman, Blandford & Rees 1980; Morgan et al. 2010; Fragione et al. 2019; Yang et al. 2019; Mannerkoski et al. 2022). When galaxies merge, the BHs at their centers, due to dynamical friction (Merritt & Milosavljevic 2005; Chen, Yu & Lu 2020), gradually move closer to each other and orbit around a common center of mass, forming a dual AGN on kpc-scale. As time goes on, gravitational wave radiation becomes the main mechanism driving the BHs further closer together, and eventually the distance between them shrinks to on sub-pc scale, forming a tightly packed BSMBH system. These two BHs may further merge to form a larger supermassive BH (SMBH), releasing strong gravitational waves at the same time (Ehlers et al. 1976;

Flanagan & Cutler 1994; Centrella et al. 2010; Hughes 2021). The study of dual AGN and BSMBHs is one of the hotspots of current research and is crucial for understanding the co-evolution of SMBHs and galaxies.

Dual AGN systems on kpc scales have been widely observed and studied through directly resolved images. However, sub-pc scale BSMBH systems have rarely been detected through directly resolved images, and the extremely close proximity between the BHs in BSMBH systems makes observation and identification very difficult through photometric images. Even with the help of high-resolution techniques such as the Very Long Baseline Interferometry Array (VLBA), only a few successes have been reported. For example, Rodriguez et al. (2006) discovered a BSMBH system within the radio galaxy 0402+379. This discovery was made possible through the use of VLBA, which provided high-resolution imaging of two compact, variable, and active nuclei within the galaxy, these nuclei with a projected separation of about 7.3 pc. In addition, Kharb, Lal & Merritt (2017) also reported another sub-pc scale BSMBH candidate with a separation of approximately 0.35 pc in NGC 7674 through VLBA.

Given the limitations of direct imaging observations, scientists have also attempted to use a variety of indirect observational methods to explore the sub-pc scale BSMBH systems in recent years. Among these, spectroscopic characterization is an important tool. For example, by observing the double-peaked features of broad emission lines in the spectra of quasars, Lauer & Boroson (2009); Shields et al. (2009); Tsalmantza et al. (2011); Eracleous et al. (2012); Shen et al. (2013); Liu et al. (2014); Runnoe et al. (2015); Wang et al. (2017) have analyzed the velocity variations of these broad emission lines. Their find-

\* E-mail: xgzhang@gxu.edu.cn

ings provide evidence supporting the probable existence of sub-pc scale BSMBH systems.

Besides the applications of unique spectroscopic features of broad emission lines, the detection of QPOs in long-term light curves is also an important and convenient indicator for identifying sub-pc scale BSMBHs candidates. Many research teams have reported the QPOs in AGN with periodicity ranging from hundreds to thousands of days. These QPOs can be caused by a variety of physical mechanisms, including jet procession (Marscher & Gear 1985; Camenzind & Krockenberger 1992; Abraham 2000; Caproni, Abraham & Monteiro 2013; Huang et al. 2021), BH tidal disruption events (Shu et al. 2020), accretion disk instabilities (Vietri & Stella 1998; Tsang & Lai 2009; Pihajoki, Valtonen & Ciprini 2013), general relativistic effects (Stella & Vietri 1998; Stella, Vietri & Morsink 1999; Ingram et al. 2016), and orbital motions of BSMBH systems (Kormendy et al. 2009; Gaskell 2010; Barth et al. 2015; Songsheng et al. 2020). Although the origin of QPOs in light curves is complex, most reported QPOs are considered to be from the orbital motions of BSMBH systems. For example, Graham et al. (2015a) detected and reported a 5.2yr periodicity in the quasar PG 1302-102, attributed to the orbital motion of a BSMBH system. In a follow-up study, Graham et al. (2015b) conducted a systematic search for QPOs in light curves of 243500 sources from the Catalina Real-Time Transient Survey (CRTS). This search led to the identification of 111 potential BSMBH candidates. The light curve characteristics of these candidates, as validated by theoretical models, were found to be consistent with the periodic variations expected from BSMBH systems. Similarly, Liu et al. (2015); Graham et al. (2015a,b); Charisi et al. (2016); Li et al. (2016); Zheng et al. (2016); Kovacevic et al. (2020); Serafinelli et al. (2020); Liao et al. (2021); O'Neill et al. (2022) have also reported sub-pc scale BSMBH candidates based on QPOs detected in the light curves. Additionally, in our recent studies on QPOs, Zhang (2022a,b, 2023b, 2025a) have also identified such BSMBH candidates in broad line AGN.

QPOs play a key role in detecting BSMBH systems in galaxies, however, relying on QPO signals for detections can present some accuracy challenges. First, the time durations of the light curves are monitored as a key factor, because the detection of QPO signals needs to rely on long-term time-series data to ensure that the observed periodic variations are not chance events. In addition, the stochastic AGN variability may produce signals similar to QPOs, as discussed in Sesana et al. (2018) and Vaughan et al. (2016). To improve the accuracy of detections of QPOs and to reduce false-positive results, it is crucial to select light curves with long-term and continuous observational data. Among the public sky surveys, the Catalina Sky Survey (CSS) (Mahabal et al. 2011; Drake et al. 2009) has sufficient temporal baseline and sky coverage to provide favorable conditions for searching for long-lived optical QPOs. In addition, the high-frequency observing capability of the Zwicky Transient Telescope (ZTF) (Bellm et al. 2019; Dekany et al. 2020) provides a finer light curve for capturing optical QPOs with shorter periods. Combining the long-term light curves of the CSS with the ZTF allows for more efficient identifications and analysis of optical QPOs. As in the recent work of Zhang (2022b, 2025a), the author combined the observations of CSS with ZTF at different time periods to obtain light-variation data up to 16 years, which provides important clues for detecting more reliable optical QPOs.

In this manuscript, through the combined light curves from CSS and ZTF, we report the discovery of a potential BSMBH system in the blue quasar SDSS J100438.8+151056 (=SDSS J1004+1510) (redshift of 0.219), which is not reported in the

sample of Graham et al. (2015b), probably due to short time duration of the CSS V-band light curve of SDSS J1004+1510 relative to its periodicity. After analyzing the CSS V-band light curve, an optical QPO signal with a periodicity around 1000 days can be detected. Moreover, QPOs with a periodicity around 220 days can be detected in the higher quality ZTF g/r-band light curves, besides the periodicity around 1000 days. The structure of this manuscript is as follows. Section 2 presents the optical QPOs through four analytical methods applied to the long-term optical light curves of SDSS J1004+1510. Section 3 focuses on the spectroscopic results. Section 4 discusses the probable central BSMBH system and the possibility of dual-periodic signals probably related to a triple BH system candidate. Finally, the conclusions are given in Section 5. In the manuscript, the cosmological parameters have been adopted as  $H_0 = 70 \text{ km} \cdot \text{s}^{-1} \text{ Mpc}^{-1}$ ,  $\Omega_\Lambda = 0.7$  and  $\Omega_m = 0.3$ .

## 2. Optical QPOs in SDSS J1004+1510

### 2.1. Long-term optical light curves of SDSS J1004+1510

The long-term light curves in observer frame of SDSS J1004+1510 can be collected from the CSS (<http://nesssi.cacr.caltech.edu/DataRelease/>) and ZTF (<https://www.ztf.caltech.edu>). The CSS V-band light curve is collected with MJD-53000 from 469 (March 2005) to 3592 (November 2013). And, the ZTF g/r band light curves are collected with MJD-53000 from the 5202 (March 2018) to 6996 (March 2023). Here, due to the ZTF i-band light curve only including 53 data points in a short time duration, it is not considered in this manuscript. The collected light curves are shown in the top left panel of Fig. 1.

### 2.2. The analyses of QPOs in SDSS J1004+1510

Similar to what we have recently done in Zhang (2022b, 2023b, 2025a), the following four methods are applied to determine the probable QPOs in SDSS J1004+1510, the direct fitting method, the phase-folded method, the Generalized Lomb-Scargle (GLS) method (Lomb 1976; Scargle 1982; Brethorst 2001; Zechmeister & Kurster 2009; VanderPlas 2018; Springford, Eadie & Thomson 2020) and the weighted wavelet Z-transform (WWZ) method (Foster 1996; An, Lu & Wang 2016; Gupta et al. 2018; Kushwaha et al. 2020; Liao et al. 2021).

The light curves are first described by the direct fitting method, with a sinusoidal function plus a fourth-degree polynomial component simultaneously applied to each light curve from the CSS and the ZTF. The sinusoidal function is specifically chosen to capture the periodic variations in the light curve, without delving into the physical origins of the QPOs, while the fourth-degree polynomial is used to represent long-term non-periodic trends. The model functions are described as follows:

$$LMC1 = A + B \times \left( \frac{t}{1000 \text{ days}} \right) + C \times \left( \frac{t}{1000 \text{ days}} \right)^2 + D \times \left( \frac{t}{1000 \text{ days}} \right)^3 + E \times \sin\left( \frac{2\pi t}{T_{QPO}} + \phi_0 \right) \quad (1)$$

While the model functions are applied, the parameter of  $T_{QPO}$  is the same for each light curve. To ensure the best fitting, the Levenberg-Marquardt least-squares method is used to optimize the parameters of these composite models. The determined model parameters are presented in Table 1, with the determined periodicity to be approximately  $985 \pm 8$  days. The best fitting results

and the corresponding 99.99994% ( $5\sigma$ ) confidence bands (determined by the F-test technique) are shown in the top left panel of Figure 1, with  $\chi^2/\text{dof} = 8847.144/827 \sim 10.69$ . The residuals (the differences between the observed data and the model predictions) are shown in the bottom left panel of Figure 1.

Besides the model functions in Equation (1), if only the fourth-degree polynomial components are used to describe each light curve, it will lead to  $\chi^2/\text{dof}_1 = 13117.669/834 \sim 15.7$ . To assess the significance of the sinusoidal components, the F-test technique is employed to compare models with and without the sinusoidal component. The F-test statistic is calculated as follows:

$$F_P = \frac{\frac{x_1^2 - x^2}{\text{dof}_1 - \text{dof}}}{x^2/\text{dof}} = 57.03 \quad (2)$$

Based on the given confidence level ( $5\sigma$ ), the numerator degree of freedom ( $\text{dof}_1 - \text{dof}$ ), and the denominator degree of freedom ( $\text{dof}$ ), the corresponding F-distribution value is calculated as:

$$F_{\text{dis}} = f_{\text{cvf}}(1 - 99.99994\%, 7, 827) = 6.3 \quad (3)$$

Therefore, through the F-test statistical technique, the sinusoidal component is preferred with a confidence level much higher than  $5\sigma$ , indicating that the periodic fluctuations in the data prefer to be a genuine feature rather than a random occurrence.

Based on the periodicity obtained from the direct fitting method, the phase-folded method is applied to the light curves after subtracting the polynomial components. Through a simple sinusoidal function by

$$LMC_{\text{ph}} = A \times \sin(2\pi t + B) + C \quad (4)$$

the folded light curves can be well described and shown in the top right panel of Figure 1, with  $\chi^2/\text{dof} = 8860.0165/843 = 10.51$ , through the Levenberg-Marquardt least-squares minimization technique. The bottom right panel of Figure 1 shows the residuals (differences between the fitting results and the phase-folded light curves).

To further investigate the optical QPOs in SDSS J1004+1510, in addition to the direct fitting method and the phase-folded method shown in Figure 1, the improved GLS method (see the python astroML package) is also applied. Compared with the traditional Lomb-Scargle method, GLS is particularly suitable for handling unevenly sampled datasets, allowing for more accurate identification and quantification of periodic signals in time series.

Figure 2 presents the GLS periodogram results for the CSS V-band and the ZTF g-band and r-band light curves. In the CSS V-band light curve, a significant peak is detected, corresponding to a periodicity about  $1250 \pm 112$ days (solid line in green), with a significance level higher than 99.99994%, along with a secondary, less prominent peak around  $272 \pm 1$ days (confidence level smaller than  $5\sigma$ ). In the GLS method results for the high quality ZTF g-band and r-band (represented by blue and red lines) light curves, there are main peaks around  $1165 \pm 30$ days and  $1000 \pm 30$ days with significance levels higher than 99.99994%. Interestingly, compared with the CSS V-band light curve, there are more prominent periodicities around  $221 \pm 2$ days and  $215 \pm 1$ days, respectively, both exceeding the 99.99994% confidence level. Based on the GLS periodogram applied to randomly created light curves including about half of the data points in the origin light curves, Figure 3 shows the distributions of peak periodicity in the CSS V-band and ZTF g-band and r-band light curves determined through the bootstrap method applied with 500 loops, leading to the determined uncertainties of the periodicities by the half width at half maximum of the distributions.

In addition, the WWZ method is also employed for an in-depth analysis of the CSS V-band and ZTF g/r-band light curves. As shown in the Figure 4, the power spectrum covered a frequency (in units of 1/days) range from 0.0005 to 0.01, with a frequency step of 0.00001. The result for the ZTF-r band light curve in the top panel reveals two distinct periodicities, one around  $950 \pm 42$ days, and another around  $270 \pm 3.5$ days. In the middle panel from the ZTF g-band light curve, two significant periodicities are also observed: one around  $1405 \pm 40$ days, and a shorter one around  $225 \pm 3$ days. While the bottom panel from the CSS-V band light curve shows a dominant periodicity around  $1265 \pm 40$ days, with a secondary periodicity around  $265 \pm 3$ days. The results obtained from the WWZ method are consistent with those derived from the GLS periodogram.

Additionally, to determine the uncertainties of the periodicities detected by the WWZ method, the bootstrap technique is applied. More than half of the data points from the observed CSS-V and ZTF g/r band light curves are randomly collected to generate new light curves, with the process repeated 800 times. Subsequently, the WWZ method is used to determine the periodic distributions of these new light curves, and the results are shown in Figure 5. The uncertainties of the periodicities were determined by the half width at half maximum of the distributions.

Based on the secondary periodicity determined by the GLS method and the WWZ method, especially in the ZTF light curves, Figure 6 shows the re-fitting results to the ZTF g-band and r-band light curves by using two sinusoidal functions. The model functions are expressed as follows:

$$\begin{aligned} LMC2 = & A + B \times \left( \frac{t}{1000 \text{ days}} \right) + C \times \left( \frac{t}{1000 \text{ days}} \right)^2 \\ & + D \times \left( \frac{t}{1000 \text{ days}} \right)^3 + E \times \sin \left( \frac{2\pi t}{T_{QPO}} + \phi_0 \right) \\ & + F \times \sin \left( \frac{2\pi t}{T_{QPO_1}} + \phi_1 \right) \end{aligned} \quad (5)$$

Then, through the Levenberg-Marquardt least-squares minimization technique, the best fitting results can be determined and shown in Figure 6 to the ZTF light curves, leading to  $\chi^2/\text{dof} = 7430.6168/728 \approx 10.206$ . The determined model parameters listed in Table 1 can be applied to support the secondary periodicities in the ZTF g/r-band light curves. Based on the model function used to fit the light curves in the left panel of Figure 1, when only the ZTF g/r bands are fitted, the resulting  $\chi^2/\text{dof}$  is calculated as  $8767.5/734 \approx 11.945$ . As demonstrated in Equation (2) and (3) above, the F-test technique is employed to compare the model containing one sinusoidal component with the model containing two sinusoidal components. The result of  $F_P$  is about  $F_P \approx 21.8$ , and the  $F_{\text{dis}}$  is about  $F_{\text{dis}} \approx 5.8$  (based on the given confidence level( $5\sigma$ )). These results indicate that the model with two sinusoidal components provides a better fit.

By applications of four different techniques, including the direct fitting method leading to the results shown in the left panel of Figure 1 and Figure 6, the phase-folded method leading to the results shown in the right panel of Figure 1, the GLS periodogram leading to the results shown in the Figure 2, and the WWZ method leading to the results shown in the Figure 4. All these methods are leading to two significant periodicities in ZTF light curves. Meanwhile, for the CSS-V band light curve, a significant periodicity is detected by four methods, while an insignificant periodicity is detected by The WWZ method and GLS. Differences in detected short-period signals between the

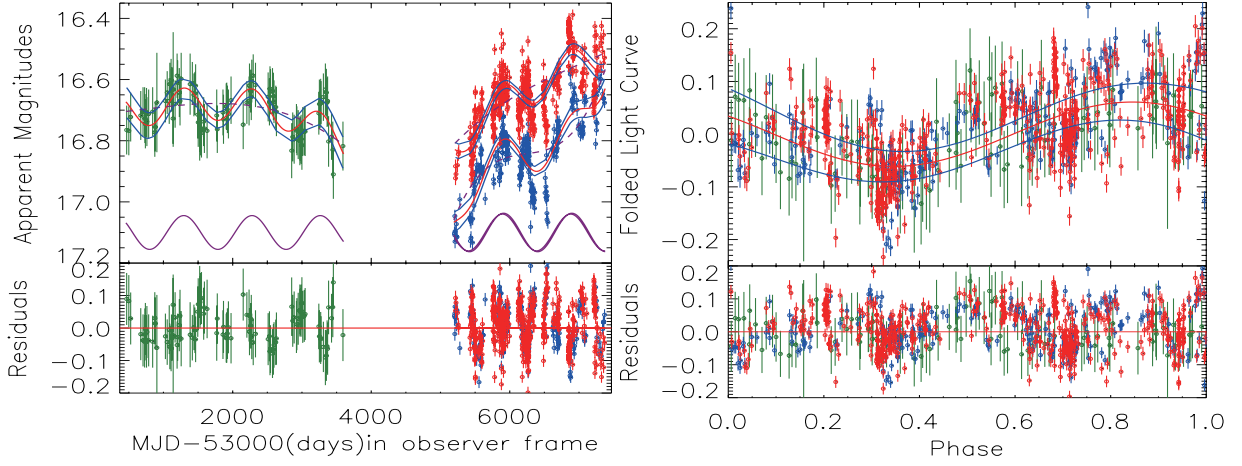


**Fig. 1.** The top left panel displays the light curves from the CSS (solid circles plus error bars in green) and from the ZTF in the g-band (minus 0.35mag) (open circles plus error bars in blue) and r-band (minus 0.35mag) (open circles plus error bars in red), alongside the best-fitting results (solid lines in red) from a sinusoidal function plus a fourth-degree polynomial component. In the top left panel, the solid purple lines represent the component described by the sinusoidal function (plus 17.5 mag), while the dashed purple lines indicate the component modeled by the polynomial function. The top right panel shows the phase-folded light curves based on the determined periodicity 985 days (with the polynomial trends subtracted; green for CSS data, blue for ZTF g-band, and red for ZTF r-band) along with the best sinusoidal fit (solid line in red). The solid blue lines in the top panels indicate the corresponding  $5\sigma$  confidence bands to the best fitting results through the F-test technique. The bottom panels display the corresponding residuals (light curves minus the best fitting results), with the solid red line denoting the residuals=0

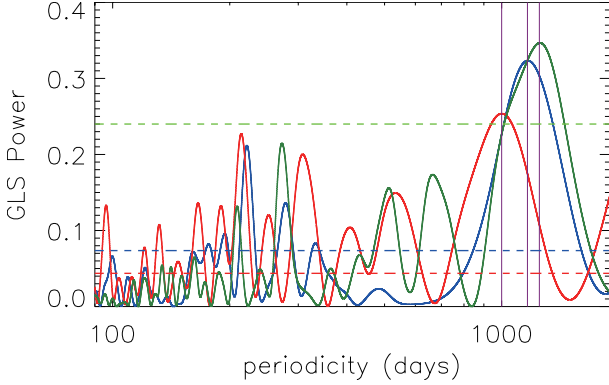


**Fig. 2.** Properties of the GLS periodogram. Solid lines in red, blue, and green show the corresponding results from the ZTF r-band, g-band, and CSS V-band light curves, respectively. The horizontal dashed lines in red, blue, and green indicate the corresponding  $5\sigma$  confidence levels (FAP = 1-99.99994%) for the results from the ZTF r-band, g-band, and CSS V-band light curves, respectively.

CSS and ZTF bands may be attributed to the higher temporal resolution and observational precision of ZTF light curves, which can reveal finer variability features that the CSS V-band might have missed. In summary, there are two periodicities in SDSS J1004+1510, at  $1103 \pm 260$ days (1103 as the mean value of the longer periodicities of 985days, 1024days, 886days, 1250days, 1165days, 1000days, 1265days, 1405days and 950days from different techniques applied to different light curves, and the uncertainty 260 as half of the maximum difference among the longer periodicities) days and  $243 \pm 29$ days (243 as the mean value of the shorter periodicities of 222days, 257days, 272days, 221days, 215days, 265days, 225days, 270days, and the uncertainty 29 as half of the maximum difference among the shorter periodicities). The source of the above periodicities is shown in table2.

### 2.3. Optical QPOs were related to intrinsic AGN variability of SDSS J1004+1510?

Similar to what we have recently done in Zhang (2023b, 2025a,b), it is necessary to check the effects of red noise traced by intrinsic AGN activities on the detected optical QPOs in SDSS J1004+1510, accepted artificial light curves  $LMC_t$  (red noises, intrinsic AGN variability) being simulated by the Continuous Autoregressive (CAR) process (Kelly,Bechtold &Siemiginowska 2009; MacLeod et al. 2010; Kozłowski et al. 2010; Zu et al. 2013):

$$dLMC_t = \frac{-1}{\tau} LMC_t dt + \sigma_c \sqrt{dt} \epsilon(t) + bdt \quad (6)$$

where  $\epsilon(t)$  is a white noise process with zero mean and variance equal to 1,  $bdt = 17.19$  is the mean value of  $LMC_t$  (with 17.19 as the mean value of the ZTF g-band light curve of SDSS J1004+1510),  $\tau$  is the relaxation time of the process, and  $\sigma$  is the variability of the time series on a timescale shorter than  $\tau$ . And the uncertainties of the simulated light curves  $LMC_t$  are given by  $dLMC_{t,err} = LMC_t + \frac{L_{err}}{L_{obs}}$ , with  $L_{obs}$  and  $L_{err}$  as the observed ZTF g-band light curve and the corresponding uncertainties, as shown in the left panel of Figure 1.

Through the CAR process in Kelly,Bechtold &Siemiginowska (2009), two sets of 10000 simulated light curves are generated. The first set had the same time information  $t$  as the actual observation time of CSS V band and ZTF g band light curves, with  $\tau$  randomly selected from 50days to 1000days and the variance  $\tau\sigma_*^2$  from 0.005 to 0.02 as the common values in quasars in MacLeod et al. (2010). The second set had the same time information as the observation time of ZTF g band light curve, with  $\tau$  from 50days to 1000days and the variance  $\tau\sigma_*^2$  from 0.005 to 0.02.

There are 15 light curves with detected QPOs that can be selected from the first set of simulated light curves, based on the following two criteria. First, the simulated light curves can be well described by Equation (1) with corresponding  $\chi^2/\text{dof}$  smaller than 15 ( $\chi^2/\text{dof}=10.69$  in Fig 1), and the determined periodicity is within the range of  $1103 \pm 260$ days. Second, the

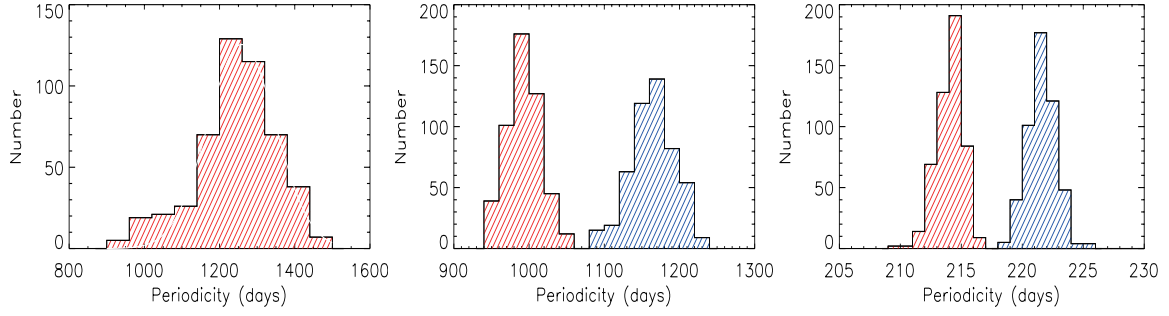


**Fig. 3.** On the periodicity distributions through the bootstrap method. The left panel shows the results for the CSS-V band light curve. The middle panel and the right panel show the periodicities for the ZTF g-band (blue histogram) around 1165days and 221days, as well as for the ZTF r-band (red histogram) around 990days and 215days.

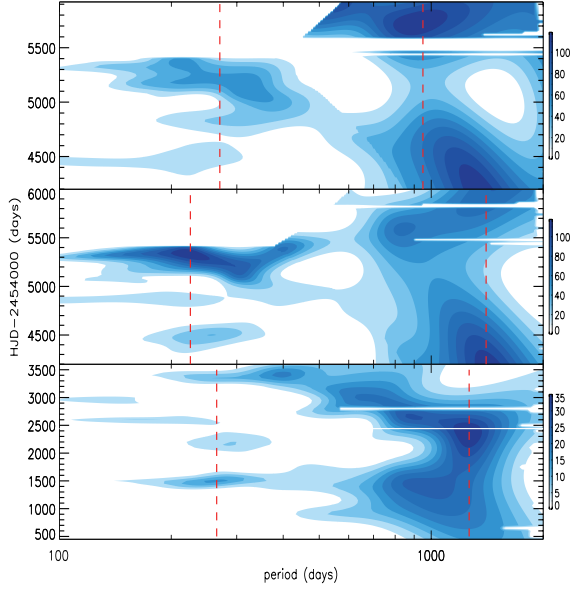


**Fig. 4.** The WWZ results for the CSS-V band and the ZTF g/r-band light curves. For the ZTF r-band light curve (top panel), two periodicities are identified at approximately  $950 \pm 42$ days and  $270 \pm 3.5$ days. For the ZTF g-band light curve (middle panel), two periodicities are around  $1405 \pm 40$ days and  $225 \pm 3$ days. For the CSS-V band light curve (bottom panel), two periodicities are around  $1265 \pm 40$ days and  $265 \pm 3$ days. In each panel, the vertical dashed red lines mark the positions for the periodicities.

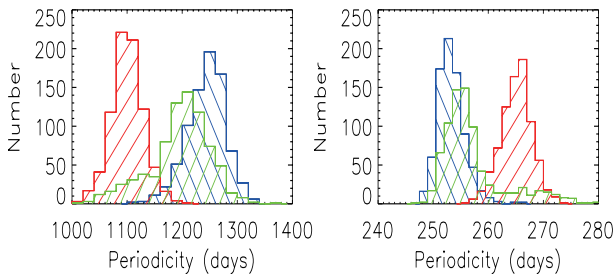


**Fig. 5.** The left and right panels present the distributions of WWZ determined periodicities around 1000days and 200days, determined by the bootstrap method. The green, blue and red histograms show the results for the CSS V-band and the ZTF g/r band light curves, respectively.

periodicity determined by the GLS method should be within  $1103 \pm 260$ days with significance level higher than  $5\sigma$ . For the second set of simulated light curves, 2 light curves with expected detected QPOs can be selected if they meet the following two

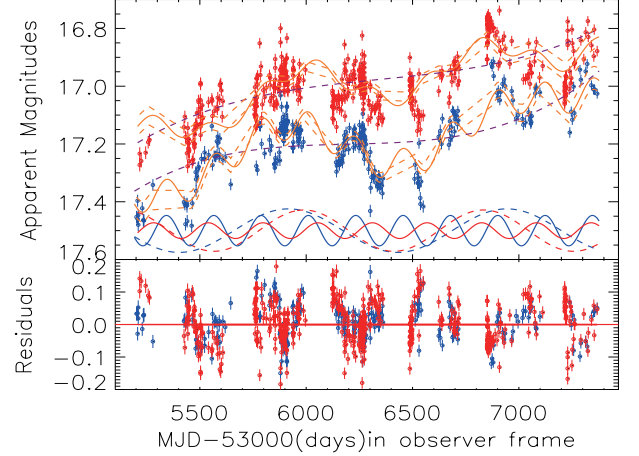


**Fig. 6.** Best fitting results (top panel) and the corresponding residuals (bottom panel) to the ZTF g/r-band light curves by two sinusoidal components. In top panel, circles plus error bars in blue and in red show the ZTF g-band and r-band light curves, the solid orange lines represent the best-fitting results, the dashed orange lines indicate the  $5\sigma$  (99.99994%) confidence bands, and the dashed purple lines show the polynomial components, the dashed blue and solid blue lines show the sinusoidal components with periods of  $1024 \pm 12$ days and  $222 \pm 1$ days in the ZTF g-band light curve, the dashed and solid lines in red represent the sinusoidal components with periods of  $886 \pm 6$ days and  $257 \pm 1$ days in the ZTF r-band light curve.

conditions. First, the simulated light curves must be well described by Equation (5) with corresponding  $\chi^2/\text{dof}$  smaller than 15 ( $\chi^2/\text{dof}=10.206$  in Fig 6), and the determined two periodicities are within  $1103 \pm 260$ days and  $243 \pm 29$ days. Second, the periodicities determined by the GLS method should be within  $1103 \pm 260$ days and  $243 \pm 29$ days, with significance level higher than  $5\sigma$ . One example of these mis-detected QPOs from each set of simulated light curves treated as red noises is shown in Figure 7.

The results above indicate that the CAR process, which can be applied to trace red noise, can lead to mis-detected QPOs in simulated light curves. However, after considering effects of red noise, it can be confirmed that the probability is only  $2/10000$  (corresponding  $3.7\sigma$ ) for two periodicities detected over the ZTF observation time, and the probability is only  $15/10000$  (corresponding  $3.17\sigma$ ) for only the large periodicity over the combined CSS and ZTF observation time. Therefore, the detected QPOs in SDSS J1004+1510 are robust enough, even after considering effects of red noise.

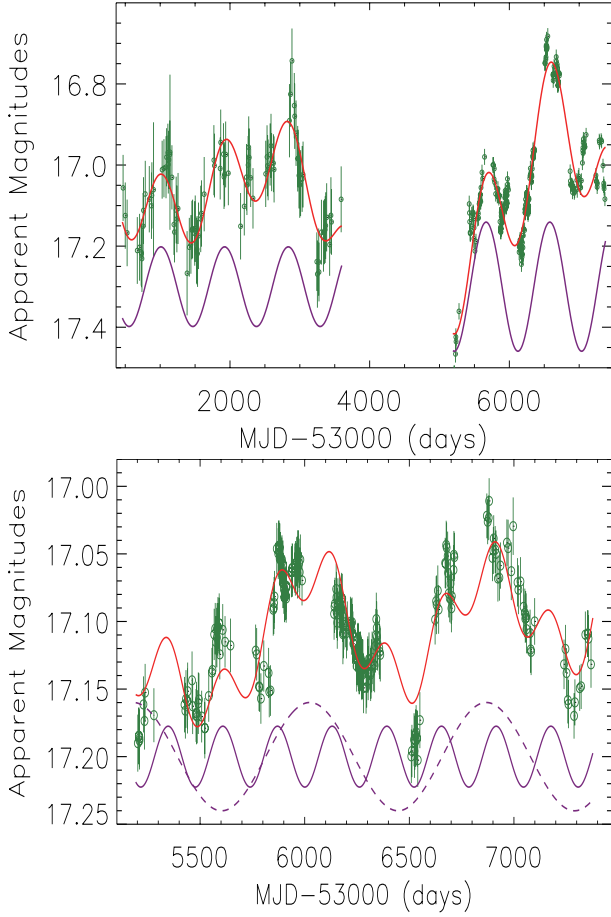


**Fig. 7.** The top panel shows an example of probable mis-detected QPOs in the first set of simulated light curves by the CAR process. Solid dark green circles plus error bars show the simulated light curve, solid lines in red show the best-fitting result by Equation(1), with  $\chi^2/\text{dof}=6$ . The solid lines in purple show the sinusoidal component with a period of 910days. The bottom panel shows one of the probable mis-detected QPOs in the second set of simulated light curves. Solid dark green circles plus error bars show the simulated light curve, solid line in red shows the best-fitting result by Equation(5), with  $\chi^2/\text{dof}=1.13$ . The solid and dashed lines in purple show the sinusoidal components with periodicity of 263days and 851days, respectively.

### 3. spectroscopic results of SDSS J1004+1510

Considering that the optical QPOs may be caused by orbital motions of two BH accreting systems in an expected central BSMBH system in SDSS J1004+1510, this orbital motions could also have probable effects on features of broad optical Balmer emission lines, if the related two broad emission line regions (BLRs) were not totally mixed. Therefore, it is necessary to study the characteristics of the broad emission lines. Figure 8 displays the SDSS spectrum of SDSS J1004+1510, collected from SDSS DR16 (Ahumada et al. 2021) with PLATE-MJD-FIBERID = 2586-54169-0405. In this spectrum, prominent emission lines can be described by multiple Gaussian functions, as demonstrated by Zhang (2022a, 2023b), which utilized a combination of broad and narrow Gaussian functions to precisely measure the emission lines.

To measure the emission lines around  $H\beta$  (rest wavelength from 4700Å to 5100Å), the following model functions are utilized. For the broad and narrow  $H\beta$  emission lines, three broad Gaussian functions and two narrow Gaussian functions (one for

**Table 1.** Parameter values for the LMC model function

LMC <sub>1</sub>	CSS-V	g band	r band
A	$16.7 \pm 0.09$	$56.2 \pm 1.74$	$21.7 \pm 1.58$
B	$-0.02 \pm 0.17$	$-18.7 \pm 0.84$	$-1.97 \pm 0.76$
C	$-0.02 \pm 0.09$	$3.02 \pm 0.13$	$0.27 \pm 0.12$
D	$0.01 \pm 0.01$	$-0.16 \pm 0.01$	$-0.01 \pm 0.01$
E	$-0.06 \pm 0.01$	$0.06 \pm 0.01$	$0.06 \pm 0.01$
$\log T_{QPO}$	$2.99 \pm 0.01$	$2.99 \pm 0.01$	$3 \pm 0.01$
$\phi_0$	$-0.39 \pm 0.22$	$-1.56 \pm 0.31$	$-1.44 \pm 0.31$
LMC <sub>2</sub>	CSS-V	g band	r band
A		$51.3 \pm 2.52$	$40.6 \pm 1.79$
B		$-16.5 \pm 1.21$	$-11.04 \pm 0.85$
C		$2.65 \pm 0.20$	$1.73 \pm 0.14$
D		$0.14 \pm 0.01$	$-0.09 \pm 0.01$
E		$0.08 \pm 0.01$	$-0.07 \pm 0.01$
$\log(T_{QPO})$		$3.01 \pm 0.01$	$2.9 \pm 0.01$
$\phi_0$		$6.02 \pm 0.48$	$-5.25 \pm 0.32$
F		$0.05 \pm 0.01$	$0.03 \pm 0.01$
$\log(T_{QPO_1})$		$2.35 \pm 0.01$	$2.41 \pm 0.01$
$\phi_1$		$-20.5 \pm 0.47$	$1.3 \pm 0.78$
LMC <sub>ph</sub>	A	B	C
	$-0.06 \pm 0.01$	$-0.60 \pm 0.02$	$-0.01 \pm 0.01$

**Notes.** The first part shows the determined parameters after applications of the model functions of LMC<sub>1</sub> in Equation (1) to the CSS and ZTF light curves. The second and the third part show the determined parameters after applications of the model functions of LMC<sub>2</sub> in Equation (5) and of LMC<sub>ph</sub> in Equation (4) to the CSS and ZTF light curves. The parameters of  $T_{QPO}$  and  $T_{QPO_1}$  are the periodicities in units of days.

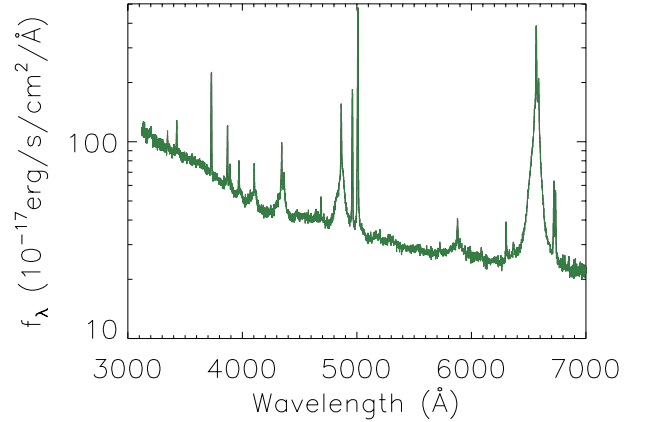


**Fig. 8.** The SDSS spectrum of SDSS J1004+1510.

the core component and the other one for the extended component) are applied. For the  $[O III] \lambda 4959\text{\AA}$ ,  $5007\text{\AA}$  doublet, three Gaussian functions are applied to each line, to describe the core component, the extended component and an additional intermediate extended component. Additionally, a power-law function is applied to describe the continuum emissions underneath the emission lines. Then, through the Levenberg-Marquardt least-squares minimization technique, the best fitting results and the corresponding residuals to the emission lines around  $H\beta$  are determined and shown in the top left panel of Figure 9 with  $\chi^2/\text{dof} = 1.1$ . Here, the corresponding residuals are determined by the spectrum minus the best fitting results, and then divided by the uncertainties of the spectrum. The determined model parameters are listed in Table 3.

**Table 2.** The periodicities original

method	CSS-V	ZTF-g	ZTF-r
direct fit	985 ± 8	*	*
direct re-fit		1024 ± 12	886 ± 6
		222 ± 1	257 ± 1
GLS	1250 ± 112	1165 ± 30	1000 ± 30
	272 ± 1	221 ± 1.5	215 ± 1
WWZ	1265 ± 40	1405 ± 40	950 ± 42
	265 ± 3	225 ± 3	270 ± 3.5

**Notes.** Repeated periodicities are not used for calculation again.

For the emission lines around  $H\alpha$  (rest wavelength from 6200Å to 6900Å), The following model functions are applied. Five Gaussian functions are applied to describe the broad and narrow  $H\alpha$  emission lines, with three Gaussian functions for the broad  $H\alpha$  and two for the narrow  $H\alpha$ . The [N II]  $\lambda 6548\text{\AA}$ , 6583Å doublet are described by four Gaussian functions for both the core and extended components. The [S II]  $\lambda 6716\text{\AA}$ , 6731Å doublet and the [O I]  $\lambda 6300\text{\AA}$ , 6363 Å doublet are also fitted in a similar manner, with one Gaussian function for core component and the other one Gaussian function for the extended component in each line. A power-law function is used for the continuum emissions underneath the emission lines. Then through the Levenberg-Marquardt least-squares minimization technique, the best fitting results and the corresponding residuals are determined and shown in the top right panel of Figure 9, with  $\chi^2/\text{dof} = 1.1$ . The determined model parameters are listed in Table 3.

To further analyze the significant physical information in the broad emission lines, the continuum and the narrow emission lines are subtracted from the spectra, leaving only the broad emission components of  $H\alpha$  and  $H\beta$ . Then, the normalized broad  $H\alpha$  and  $H\beta$  are shown in velocity space in Figure 10, to show line profile comparisons between broad  $H\alpha$  and broad  $H\beta$  in SDSS J1004+1510. Meanwhile, based on the second moment definition of emission lines (Peterson et al. 2004), the measured line widths of the broad  $H\alpha$  and broad  $H\beta$  are  $2677.8 \pm 539$  km/s and  $1871.67 \pm 441.24$  km/s (the uncertainty determined by the maximum error of  $\sigma$  for the broad Gaussian components in Table 3), respectively. It is evident that the line width of broad  $H\alpha$  is a bit greater than that of broad  $H\beta$ . However, as noted by Korista & Goad (2004); Bentz et al. (2010); Netzer (2020), broad  $H\alpha$ , having the largest intrinsic optical depth among the broad Balmer emission lines, would typically exhibit a narrower (or similar, but not larger) line width than of broad  $H\beta$ . This suggests that intrinsic optical depth differences alone cannot explain the observed line profile variations. As proposed by Zhang (2023a), the distinct line profiles of broad Balmer emission lines are likely due to extrinsic obscuration differences between the two independent broad-line regions of the BSMBH system, providing support for the presence of central BSMBHs. Additionally, the peak velocities (relative to the rest-frame central wavelength) of  $H\alpha$  and  $H\beta$  are approximately  $-85.59 \pm 110.59$  km/s and  $241.18 \pm 543$  km/s, respectively (the uncertainty determined by the maximum error of  $\lambda_0$  for the broad Gaussian components in Table 3). The significant shifted velocity difference also implies that if the broad  $H\alpha$  and broad  $H\beta$  originated from the probably different regions otherwise similar kinematic system should lead to similar peak velocities and similar line widths (second moment). Therefore, the results above suggest the possible existence of two broad emission line regions.

**Table 3.** Line parameters

line	$\lambda_0$	$\sigma$	flux
Broad $H\alpha$	6556.3 ± 0.5	41.6 ± 0.6	6842 ± 167
	6560.5 ± 2.4	106.8 ± 4.9	2663 ± 125
	6574.7 ± 0.4	17.5 ± 0.4	2956 ± 127
Broad $H\beta$	4868.7 ± 1.1	16.9 ± 1.2	1549 ± 207
	4825.8 ± 3.2	19.6 ± 1.9	679 ± 103
	4909.5 ± 8.8	22.1 ± 4.8	365 ± 140
Narrow $H\alpha$	6566.3 ± 0.1	2.7 ± 0.1	1592 ± 55
	6559.6 ± 0.6	2.3 ± 0.4	149 ± 44
Narrow $H\beta$	4863.9 ± 0.1	2.0 ± 0.1	403 ± 15
	4859.2 ± 0.4	1.7 ± 0.3	54 ± 13
[O III] $\lambda 5007\text{\AA}$	5009.3 ± 0.1	2.0 ± 0.1	1442 ± 122
	5007.2 ± 0.3	3.1 ± 0.1	1406 ± 126
	5009.2 ± 0.5	12.6 ± 0.6	402 ± 18
[O I] $\lambda 6300\text{\AA}$	6303.2 ± 0.2	2.5 ± 0.2	74 ± 7
	6307.5 ± 1.8	10.6 ± 1.9	53 ± 12
[O I] $\lambda 6363\text{\AA}$	6366.6 ± 0.2	2.5 ± 0.2	21 ± 5
	6371.1 ± 1.8	10.7 ± 1.9	42 ± 12
[S II] $\lambda 6716\text{\AA}$	6719.9 ± 0.1	2.7 ± 0.1	222 ± 13
	6725.4 ± 1.3	10.9 ± 1.1	137 ± 26
[S II] $\lambda 6731\text{\AA}$	6734.3 ± 0.1	2.7 ± 0.1	180 ± 12
	6739.8 ± 1.3	10.9 ± 1.1	0*
[N II] $\lambda 6583\text{\AA}$	6586.9 ± 0.1	2.7 ± 0.1	491 ± 23
	6580.6 ± 0.6	2.3 ± 0.4	49 ± 19
line	$\lambda_0$	$\sigma$	flux
Broad $H\alpha$	6562 ± 0.3	39.4 ± 0.5	7610 ± 140
	6543 ± 2.3	93.1 ± 3.3	2750 ± 145
Broad $H\beta$	4867.6 ± 0.5	25.0 ± 0.4	2108 ± 39
	4815.3 ± 1.2	13.7 ± 1.1	288 ± 32
Narrow $H\alpha$	6566 ± 0.1	3.9 ± 0.1	2436 ± 36
	65560 ± 0.5	3.9 ± 0.4	0*
	6557 ± 0.6	2.8 ± 0.6	86 ± 23
Narrow $H\beta$	4863.7 ± 0.1	1.6 ± 0.1	154 ± 16
	4857.1 ± 0.2	2.2 ± 0.1	27 ± 7
	4863.8 ± 0.1	3.0 ± 0.1	346 ± 21
[O III] $\lambda 5007\text{\AA}$	5009.3 ± 0.1	2 ± 0.2	1402 ± 122
	5007.2 ± 0.2	3.1 ± 0.1	1438 ± 126
	5008.3 ± 0.4	12.5 ± 0.6	396 ± 18
[O I] $\lambda 6300\text{\AA}$	6303.1 ± 0.2	3 ± 0.2	98 ± 5
	6314.3 ± 0.9	3.4 ± 1	21 ± 5
[O I] $\lambda 6363\text{\AA}$	6366.6 ± 0.2	3.0 ± 0.2	35 ± 4
	6377.9 ± 1.8	13.4 ± 1	10 ± 4
[S II] $\lambda 6716\text{\AA}$	6719.9 ± 0.1	2.9 ± 0.1	239 ± 9
	6724 ± 1.6	17.9 ± 1.1	196 ± 24
[S II] $\lambda 6731\text{\AA}$	6734.3 ± 0.1	2.8 ± 0.1	192 ± 8
	6738.4 ± 1.3	18 ± 1.1	0*
[N II] $\lambda 6583\text{\AA}$	6586.9 ± 0.1	4 ± 0.1	1063 ± 26
	6577.5 ± 0.5	2.8 ± 0.4	284 ± 25

**Notes.** The first column shows which line is measured. The second, third, fourth column show the measured line parameters: the center wavelength  $\lambda_0$  in units of Å, the line width (second moment)  $\sigma$  in units of Å and the line flux in units of  $10^{-17}$  erg/s/cm<sup>2</sup>.

The first part presents the parameters when the broad Balmer lines are fitted with three broad Gaussians, and the second part presents the parameters when fitted with two broad Gaussians.

For [S II]  $\lambda 6731\text{\AA}$ , there are two Gaussian components applied, but only one reliable Gaussian component is determined and shown in the right panels of Figure 9

For the second part of the narrow  $H\alpha$ , there are three Gaussian components applied, but only two reliable Gaussian components are determined and shown in the bottom right panel of Figure 9

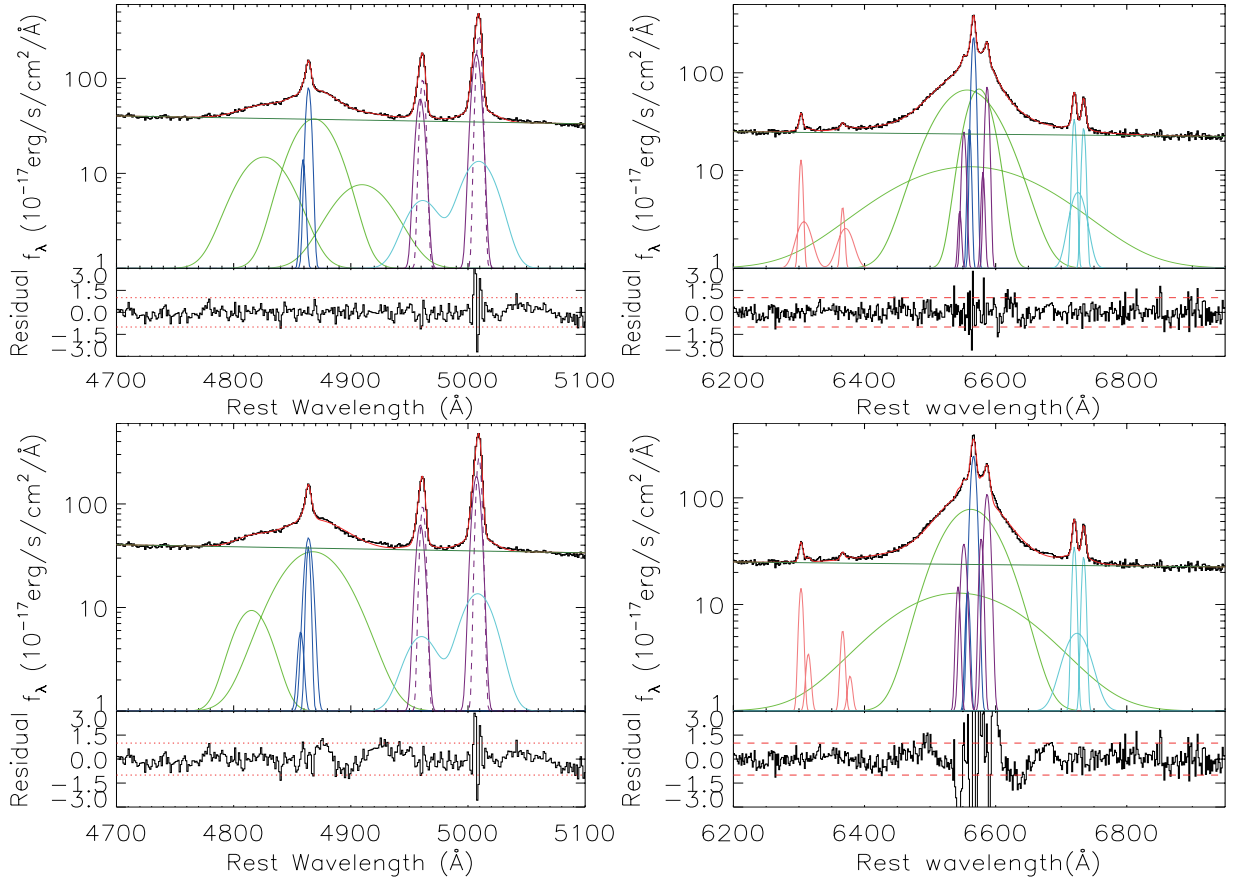


**Fig. 9.** The top panels show the fitting results and the corresponding residuals for the emission lines around  $H\beta$  and  $H\alpha$ , respectively, considering three broad Gaussian components for broad Balmer lines. In the top left panel, the solid black line represents the observed SDSS spectrum, the solid red line indicates the best fitting results, the green and blue lines show the broad and narrow  $H\beta$  components, the solid cyan and purple lines represent the core and extended components of the  $[O\ III]$  doublet. In the top right panel, the solid black line represents the observed SDSS spectrum, the solid red line represents the best fitting results, the solid green line illustrates the broad Gaussian components of  $H\alpha$ , the solid blue line represents the narrow Gaussian components in  $H\alpha$ , the solid purple line shows the core and extended components of the  $[N\ II]$  doublet, the solid cyan line represents the core and extended components in the  $[S\ II]$  doublet, the solid pink line indicates the core and extended components in the  $[O\ I]$  doublet. In each top panel, the dashed green line represents the determined power-law continuum emissions. For each residuals, the horizontal dashed red lines show residuals  $=\pm 1$ . In order to show clear features of the determined emission components, the plots are shown with y-axis in logarithmic. Similar to the results presented in top panels, bottom panels show the fitting results and the corresponding residuals for the emission lines around  $H\beta$  and  $H\alpha$ , respectively, considering two broad Gaussian components for broad Balmer lines.

Furthermore, the intensity ratio of the broad  $H\alpha$  to broad  $H\beta$  can be calculated as 4.83, a bit larger than the theoretical value of 2.86, indicating that dust extinction might be present in the BLRs of SDSS J1004+1510, causing more absorption of  $H\beta$ . However, while dust extinction could explain the larger intensity ratio than 2.86, it alone is insufficient to account for the velocity and profile differences between the broad  $H\alpha$  and broad  $H\beta$ . Moreover, differences in optical depth may partially contribute to the differences in the profiles of broad  $H\alpha$  and broad  $H\beta$ , but they cannot solely explain the significant velocity shifts between broad  $H\alpha$  and broad  $H\beta$ .

In conclusion, the hypothesis of a BSMBH system is a more reasonable explanation: broad  $H\alpha$  and broad  $H\beta$  originate from two distinct BLRs. Future work will require long-term spectral monitoring to search for periodic red-shifted and blue-shifted features, multi-wavelength observations to analyze dust distribution, and kinematic modeling to further confirm the existence of this BSMBH system.

## 4. discussion

### 4.1. Discussions on the expected BSMBH system

If there was an expected BSMBH system in SDSS J1004+1510, the discussion of BH mass becomes crucial. Typically, the virial mass of the BH can be estimated from the properties of two broad components in the broad Balmer lines. In this case, the  $H\beta$  and  $H\alpha$  lines are refitted with two prominent Gaussian components and three narrow Gaussian components, respectively. The fitting results are shown in bottom panels of Figure 9, and the determined parameters are listed in Table 3. Here, we should note that the main purpose of the refitted results is only to check dynamical properties under the assumption that there were two independent BLRs related to each BH accretion system in the expected BSMBH system in SDSS J1004+1510. Moreover, as shown in bottom panels of Figure 9 and the determined parameters listed in Table 3, one of the two determined broad components in broad  $H\alpha$  has no shifted velocities, therefore, the determined parameters of the two broad Gaussian components in broad  $H\beta$  are mainly considered as follows.

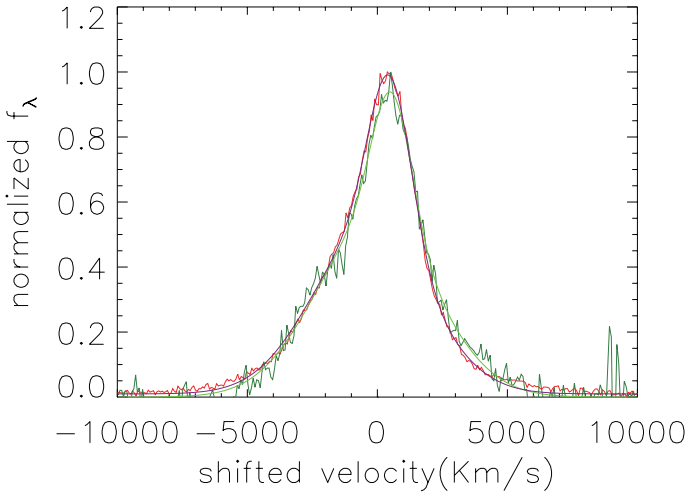


**Fig. 10.** Line profile Comparisons of broad H $\alpha$  (in red) and broad H $\beta$  (in green) in velocity space, after subtracting the continuum and all other narrow emission lines.

If the refitted two broad components do originate from two independent BLRs, the masses of the two BHs in the central BSMBH system can be estimated as follows. According to the virial theorem, the kinetic energy of the gas cloud balances with its gravitational potential energy (Peterson et al. 2004; Vestergaard & Peterson 2006). Combining this with the empirical R-L relation (Wandel, Peterson & Malkan 1999; Kaspi et al. 2000; Bentz et al. 2013), which shows a strong linear correlation between the size of the BLRs and the optical continuum luminosity (or the broad line luminosity), the virial BH mass can be expressed as (Peterson et al. 2004; Greene & Ho 2005):

$$\frac{M_{BH}}{M_{\odot}} = 2.2 \times 10^6 \times \left( \frac{L_{H\beta}}{10^{42} \text{ erg/s}} \right)^{0.56} \times \left( \frac{FWHM_{H\beta}}{1000 \text{ km/s}} \right)^{2.06} \quad (7)$$

with the line widths and the line luminosities of the two broad Gaussian components of the H $\beta$ , the masses of the redshifted and blueshifted BH systems are determined to be  $m_{BHr} = (5.8 \pm 0.28) \times 10^7 M_{\odot}$  and  $m_{BHb} = (5.49 \pm 1.37) \times 10^6 M_{\odot}$ , respectively.

The mass of redshifted BH system is far greater than that of the blueshifted BH system. In this case, the orbital separation between the two BHs can be simply estimated according to Kepler's laws, with the blueshift velocity and the mass of the primary SMBH:

$$r = \frac{GM_{BHr}}{(V_b)^2} \approx (9.55 \pm 1.2) \times 10^{14} \text{ m} = (1.12 \pm 0.14) \times 10^4 R_G \quad (8)$$

Subsequently, the orbital period can be calculate as:

$$T = \sqrt{\frac{4\pi^2 r^3}{GM_{BHr}}} \approx (2.1 \pm 0.4) \times 10^9 \text{ s} = 66.9 \pm 1.2 \text{ yr} \quad (9)$$

The orbital period is approximately 66.9 years, showing a certain discrepancy with the detected optical QPOs in SDSS J1004+1510. However, this discrepancy may stem from the unreliable re-fitting of the two prominent Gaussian components for the broad Balmer lines, especially when compared to the three components model. The  $\chi^2/\text{dof}$  value of the two components model is higher than that of the three components model ( $1.8 > 1.1$ ), and the residuals of the two components model are larger and more scattered. In addition, the discrepancy may also result from the mixing of BLRs, where the two broad components

may not originate from two independent BLRs. As a result, the calculated results may not be fully reliable based on these two broad components. therefore, the virial mass of the BH estimated from the properties of two broad components is not used in this manuscript.

Instead, the BH mass is determined based on the broad Balmer lines using Equation 7 considering the line parameters determined by three Gaussian functions to describe the broad Balmer lines, with the line luminosity of total broad H $\alpha$   $L_{H\alpha} \sim (1.76 \pm 0.05) \times 10^{43} \text{ erg/s}$  and of total broad H $\beta$   $L_{H\beta} \sim (0.37 \pm 0.06) \times 10^{43} \text{ erg/s}$  and FWHM of total broad H $\alpha$   $FWHM_{H\alpha} \sim 3102 \pm 155 \text{ km/s}$  and of total broad H $\beta$   $FWHM_{H\beta} \sim 2936 \pm 150 \text{ km/s}$ , the virial BH masses can be calculated as  $M(\text{BH}, H\alpha) \sim (1.13 \pm 0.14) \times 10^8 M_{\odot}$  and  $M(\text{BH}, H\beta) \sim (4.17 \pm 0.9) \times 10^7 M_{\odot}$ . There is an obvious difference in the BH mass derived from broad H $\alpha$  and broad H $\beta$ , to re-confirm the different kinematic properties (or different line profiles) between broad H $\alpha$  and broad H $\beta$  to support the central BSMBHs in SDSS J1004+1510. Generally, the BH mass estimation by H $\alpha$  is more reliable due to its lesser susceptibility to dust extinctions.

Subsequently, the spatial separation between the two black holes can be further estimated based on total BH mass of a BSMBH system. The specific formula is as follows (Eracleous et al. 2012):

$$A_{BSMBH} = 0.432 \times M_8 \times \left( \frac{P_{BSMBH}/\text{yr}}{2652 M_8} \right)^{2/3} \quad (10)$$

with  $M_8 = \frac{M_{BH}}{10^8 M_{\odot}}$  and  $P_{BSMBH}$  as the orbital periodicity of the BSMBH system. Accepted the  $P_{BSMBH} \sim 3.02 \pm 0.71 \text{ yr}$  ( $1103 \pm 260$  days) and  $M(\text{BH}, H\alpha)$  as the total BH mass, the orbital separation can be estimated to be  $A_{BSMBH} \sim (0.0053 \pm 0.0016) \text{ pc} \sim 6.3 \pm 1.9 \text{ light-days}$ . Meanwhile, based on the empirical R-L relation  $R_{BLR} \propto L_{5100}^{1/2}$  with the continuum luminosity  $L_{5100} = (2.36 \pm 0.08) \times 10^{44} \text{ erg/s}$  at  $5100 \text{ \AA}$ , the estimated  $R_{BLR}$  is  $57 \pm 1 \text{ light-days}$  which is greater than the orbital separation  $A_{BSMBH}$ . It means that the two BLRs related to each BH accreting system in the supposed BSMBH system should be partly (or totally) mixed in SDSS J1004+1510. Therefore, there are no apparent double-peaked features in the broad Balmer emission lines in SDSS J1004+1510. Moreover, if the two BLRs were not totally mixed, periodic variability of the central wavelengths of the broad Balmer emission lines could be expected. In the future, using multi-epoch spectroscopic observations to search for velocity.

Besides the preferred BSMBH system in SDSS J1004+1510, the other explanations are discussed as follows for the optical QPOs in SDSS J1004+1510, such as disk precession and jet precessions.

In Asahina & Ohsuga (2024), large-scale radiation electromagnetic simulations were conducted, providing the first evidence that the precession phenomenon of super-strong accretion disks is driven by the rotation of the black hole. This precession leads to periodic variation in the direction of radiation of the accretion disk at different times. To explain the optical QPOs in SDSS J1004+1510, the disc precession model discussed in Eracleous, Livio & Halpern (1995) and Bergmann et al. (2003) has been accepted, leading to the expected periodicity as

$$T_{\text{pre}} \approx 1040 M_8 R_3^{2.5} \text{ yr} \quad (11)$$

where  $R_3$  (in units of  $10^3 R_G$ ) represents the distance from the optical emission region to the central BH. Substituting the periodicity  $T \approx 3.02 \pm 0.71 \text{ yr}$  ( $1103 \pm 260$  days), along with the BH

mass  $M(\text{BH}, H\alpha) \sim (1.13 \pm 0.14) \times 10^8 M_\odot$ , the corresponding  $R_3$  can be calculated to be  $0.092 \pm 0.0036$ , indicating the distance  $R_{opt}$  about  $92 \pm 3.6 R_G$  of the optical emission regions to central BH in SDSS J1004+1510.

Meanwhile, the distance of the near-ultraviolet (NUV) emission region to the central BH also can be estimated well by using the following formula (Morgan et al. 2010):

$$\log R_{2500} = 15.78 + 0.80 \log \left( \frac{M_{\text{BH}}}{10^9 M_\odot} \right) \quad (12)$$

The calculation shows that the distance of the NUV emission regions to central BH in SDSS J1004+1510 is approximately  $(1.05 \pm 0.1) \times 10^{15}$  cm, which corresponds to about  $R_{UV} \sim 63 \pm 2 R_G$  ( $R_G = \frac{GM_{\text{BH}}}{c^2}$ ). It is smaller than the  $R_{opt}$  calculated by the disk precession model. Therefore, the disk precession model can not be ruled out in SDSS J1004+1510.

However, if the disk precession was preferred in SDSS J1004+1510, different periodicities in different epochs could be expected in SDSS J1004+1510. For the ZTF light curves which are brighter than the CSS V-band light curve, simply indicating that the distance of optical emission regions to central BH during the period for ZTF g/r-band light curves should be longer than the distance during the period for the CSS V-band light curve, therefore larger periodicity should be expected in the ZTF g/r-band light curves. However, as shown in Figure 2, the periodicities in the ZTF light curves are smaller than that in the CSS light curve. Therefore, the disk precession is not preferred in SDSS J1004+1510. In the near future, to check optical QPOs in different epochs could provide further clues to support or to rule out the disk precession in SDSS J1004+1510.

Furthermore, jet precession is one of the potential mechanisms for QPOs. Because the jet has a helical structure (Bhatta 2018), there is a periodic change in the angle between its radiation direction and the observed line of sight, so that periodic variability can be observed, such as there is a periodicity about 47 days in 3C 454.3 was reported by Sarkar et al. (2021). Like what has been done in the work of Kellermann et al. (1989), the radio-optical luminosity ratio  $R$  can be used to identify the type of radio source, with the specific formula

$$R = \frac{\frac{f_r \times 5 \text{ GHz}}{10^{26} \text{ erg/s/Hz/cm}^2}}{\frac{f_{5100} \times 5100}{\text{erg/s/cm}^2/\text{\AA}}} \quad (13)$$

with  $f_r$  (3.19 mJy) the peak radio flux intensity at 5GHz, collected from the FIRST (Faint Images of the Radio Sky at Twenty-cm) (Becker, White & Helfand 1995; Helfand, White & Becker 2015) (<http://sundog.stsci.edu/cgi-bin/searchfirst>), and  $f_{5100}$  denoting the optical flux density at 5100Å,  $33.43 \times 10^{-17} \text{ erg/s/cm}^2/\text{\AA}$ . We can find  $R = 4.08 \times 10^{-2}$ , indicating that SDSS J1004+1510 is a radio quiet object without significant jet activities. Thus, based on its radio properties, jet precession can be ruled out as the cause of the QPOs in SDSS J1004+1510.

#### 4.2. Sub-pc triple BH system candidate related to QPOs with two periodicities

In the section above, as shown in Figure 6,4, a comprehensive analysis of multi-band light curves, combined with cross-verification using multiple methods, confirmed the presence of QPOs in SDSS J1004+1510 with a periodicity about  $1103 \pm 260$  days. However, besides the prominent periodicity around 1103 days, there is a secondary periodicity about  $243 \pm 29$  days in the more refined ZTF light curve data.

The ratio between these two periodicities is approximately  $4.54 \pm 0.47$  showing an intriguing near-multiple relationship. This relationship may imply the existence of harmonic oscillations within the system, though limitations in current observational capabilities make it challenging to definitively identify which periodicity represents the true QPO signals.

However, if both periodicities represent independent QPO phenomena, as there are few harmonic oscillations in the reported optical QPOs. In this case, the system might be a triple BH system, where gravitational interactions among the three black holes generate a complex dynamical structure. If assuming a triple BH system including a sub-pc BSMBH system and a third BH far away from the BSMBH system, some basic structure information can be simply estimated. Accepted the total BH mass of  $M(\text{BH}, H\alpha) \approx (1.13 \pm 0.14) \times 10^8 M_\odot$ , the larger orbital separation corresponding to the  $1103 \pm 260$  days periodicity is approximately  $0.0053 \pm 0.0016$  pc. If accepted the total BH mass of the sub-pc BSMBH system and the third BH each account for half of the total BH mass, the smaller orbital separation associated with the  $243 \pm 29$  days periodicity is  $0.00036 \pm 0.00004$  pc for the sub-pc close BH pair.

Actually, despite the near-multiple characteristic observed between the two periods, limitations in current observational results make it difficult to clearly distinguish which of these periods represents the true QPO signal in the system.

## 5. Summary and Conclusions

The final summary and main conclusions are as follows.

- A sinusoidal fit has been conducted on the light curves of CSS V-band and ZTF g/r-band of SDSS J1004+1510, identifying a periodicity about  $985 \pm 8$ . The F-test technique can be applied to confirm the significance of the sinusoidal component with a confidence level higher than  $5\sigma$  (99.99994%). Phase-folded light curves further supported the presence of optical QPOs.
- When analyzing ZTF g-band and r-band light curves independently, dual sinusoidal fits determined periodicity are  $1024 \pm 12$  days and  $222 \pm 1$  days in the ZTF g-band light curve,  $884 \pm 6$  days and  $257 \pm 1$  in the ZTF r-band light curve.
- According to GLS method, the periodicity in the CSS-V band light curve is  $1250 \pm 112$  days, with a confidence level higher than  $5\sigma$ . For the ZTF g-band light curve, there are two periodicities with confidence level higher than  $5\sigma$ ,  $1165 \pm 30$  days and  $221 \pm 1.5$  days. And for the r-band light curve, there are also two periodicities with confidence level higher than  $5\sigma$ ,  $1000 \pm 30$  days and  $215 \pm 1$  days. The bootstrap methods further verifies the robustness of periodic testing.
- The WWZ method validates the periodicities of  $1405 \pm 40$  days and  $225 \pm 3$  days in the ZTF g-band, as well as  $950 \pm 42$  days and  $270 \pm 3.5$  days in the r-band light curve. While a  $1265 \pm 40$  days periodic signal in the CSS-V band, the result is basically the same as those of the GLS method.
- The two periodicities in SDSS J1004+1510 are not related to intrinsic AGN activities, as confirmed by simulated light curves using the CAR process, with a significance level higher than  $3.17\sigma$ .
- Analysis of the  $H\alpha$  and  $H\beta$  broad emission line profiles of SDSS J1004+1510 yields a central virial BH mass of  $(1.13 \pm 0.14) \times 10^8 M_\odot$ .
- Based on the virial BH mass and optical periodicity, the estimated separation for two BHs is approximately  $A_{\text{BSMBH}} \sim 0.0053 \pm 0.0016$  pc, if accepted BSMBH system in SDSS J1004+1510.

- Further analysis can lead the estimated size of the near-UV emitting region to be around  $63 \pm 2R_G$ , it is one third times smaller than the size of optical emitting regions ( $92 \pm 3.6R_G$ ) calculated according to the disk precession model. It is hard to rule out the disk precession leading to the optical QPOs in SDSS J1004+1510. However, due to smaller periodicities in the ZTF light curves than that in the CSS light curve, the disk precession is not preferred in SDSS J1004+1510.
- The peak radio flux of SDSS J1004+1510 is 1.39 mJy at 5GHz, leading SDSS J1004+1510 as a radio quiet AGN. Therefore, the jet precession can be totally ruled out for the QPOs in SDSS J1004+1510.
- For the source of multi-periodic QPO signals, two possibilities are proposed: one is that they may be harmonic signals generated by base frequency oscillations. Another one is that there is a triple black hole system. Future observations will provide further information to verify the origin of multi-periodic QPOs in SDSS J1004+1510.

## Acknowledgements

The authors gratefully acknowledge the anonymous referee for giving us constructive comments and suggestions to greatly improve the paper. Zhang gratefully acknowledges the kind grant support from NSFC-12173020 and NSFC-12373014. This paper has made use of the data from the SDSS projects, <http://www.sdss3.org/>, managed by the Astrophysical Research Consortium for the Participating Institutions of the SDSS-III Collaboration. This paper has made use of the data from the ZTF <https://www.ztf.caltech.edu> and from the CSS <http://nesssi.cacr.caltech.edu/DataRelease/>. The paper has made use of the MPFIT package <https://pages.physics.wisc.edu/~craigm/idl/compfit.html>. This research has made use of the NASA/IPAC Extragalactic Database (NED, <http://ned.ipac.caltech.edu>) which is operated by the California Institute of Technology, under contract with the National Aeronautics and Space Administration.

## References

- An, T.; Lu, X.; Wang, J., 2016, *A&A*, 585, 89  
 Abraham, Z., 2000, *A&A*, 355, 915  
 Ahumada, R.; Prieto, C. A.; Almeida, A.; et al., 2021, *ApJS*, 249, 3  
 Asahina, Y.; Ohsuga, K., 2024, *ApJ*, 973, 45  
 Bentz, M. C.; Kelly, D. D.; Catherine, J. G.; et al., 2010, *ApJ* 716 993  
 Bundy, K.; Fukugita, M.; Ellis, R. S.; Targett, T. A.; Belli, S.; Kodama, T., 2009, *ApJ*, 697, 1369  
 Bottrell, C.; Hani, M. H.; Teimoorinia, H.; et al., 2019, *MNRAS*, 490, 5390  
 Begelman, M. C.; Blandford, R. D.; Rees, M. J., 1980, *Natur*, 287, 307  
 Barth, A. J.; Bennert, V. N.; Canalizo, G.; et al., 2015, *ApJS*, 217, 26  
 Bergmann, T. S.; Silva, R. N.; Eracleous, M.; et al., 2003, *ApJ*, 598, 956  
 Bellm, E. C.; Kulkarni, S. R.; Barlow, T.; et al., 2019, *PASP*, 131, 068003  
 Bretthorst, G. L., 2001, *AIPC*, 568, 241  
 Becker, R. H.; White, R. L.; Helfand, D. J., 1995, *ApJ*, 450, 559  
 Bentz, M. C.; Denney, K. D.; Grier, C. J.; et al., 2013, *ApJ*, 767, 149  
 Bhatta, G., 2018, *Galaxy*, 6, 136  
 Barnes, J. E.; Hernquist, L., 1996, *ApJ*, 471, 115  
 Carlberg, R. G., 1992, *ApJL*, 399, L31  
 Chen, Y. F.; Yu, Q. J.; Lu, Y. J., 2020, *ApJ*, 897, 86  
 Centrella J.; Baker, J. G.; Kelly, B. J.; van Meter, J. R., 2010, *RvMP*, 82, 3069  
 Camenzind, M.; Krockenberger, M., 1992, *A&A*, 255, 59  
 Caproni, A.; Abraham, Z.; Monteiro, H., 2013, *MNRAS*, 428, 280  
 Charisi, M.; Bartos, I.; Haiman, Z.; Price-Whelan, A. M.; Graham, M. J.; Bellm, E. C.; Laher, R. R.; Marka, S., 2016, *MNRAS*, 463, 2145  
 Drake, A. J.; Djorgovski, S. G.; Mahabal, A.; et al., 2009, *ApJ*, 696, 870  
 Dekany, R.; Smith, R. M.; Riddle, R.; et al., 2020, *PASP*, 132, 038001  
 Eracleous M., Boroson T. A., Halpern J. P., Liu J., 2012, *ApJS*, 201, 23  
 Eracleous, M.; Livio, M.; Halpern, J. P., 1995, *ApJ*, 438, 610  
 Ehlers, J.; Rosenblum, A.; Goldberg, J. N.; Havas, P., 1976, *ApJL*, 208, L77  
 Foster, G., 1996, *AJ*, 112, 1709  
 Ferrarese, L.; Ford, H., 2005, *Space Sci. Rev.*, 116, 523  
 Fragnone, G.; Grishin, E.; Leigh, N. W. C.; Perets, H. B.; Perna, R., 2019, *MNRAS*, 488, 47  
 Flanagan, E. E.; Cutler, C., 1994, *PhRvD*, 49, 2658  
 Gaskell, C. M., 2010, *Natur*, 463, E1  
 Graham, M. J.; Djorgovski, S. G.; Stern, D.; et al., 2015a, *Natur*, 518, 74  
 Graham, M. J.; Djorgovski, S. G.; Stern, D.; et al., 2015b, *MNRAS*, 453, 1562  
 Gupta, A. C.; Tripathi, A.; Wiita, P. J.; et al., 2018, *A&A*, 616, 6  
 Greene, J. E.; Ho, L. C., 2005, *ApJ*, 630, 122  
 Heckman, T. M.; Best, P. N., 2014, *ARA&A*, 52, 589  
 Hughes, S. A., 2009, *ARA&A*, 47, 107  
 Huang, S. F.; Yin, H. X.; Hu, S. M.; Xu, C.; Jiang, Y. G.; Alexeeva, S.; Wang, Y. F., 2021, *ApJ*, 922, 222  
 Helfand, D. J.; White, R. L.; Becker, R. H., 2015, *ApJ*, 801, 26  
 Ingram, A.; van der Klis, M.; Middleton, M.; et al., 2016, *MNRAS*, 461, 1967  
 Jackson, R. A.; Kaviraj, S.; Martin, G.; et al., 2021, *MNRAS*, 506, 4499  
 Korista, K. T.; Goad, M. R., 2004, *ApJ*, 606, 749  
 Kauffmann, G.; White, S. D. M.; Guiderdoni, B., 1993, *MNRAS*, 264, 201  
 Kim, D.; Kyeong, S. Y.; Jaffe, Y. L.; et al., 2024, *ApJ*, 966, 124  
 Kormendy, J.; Richstone, D., 1995, *ARA&A*, 33, 581  
 Kormendy, J.; Ho, L. C., 2013, *ARA&A*, 51, 511  
 Kovacevic, A. B.; Yi, T. F.; Dai, X. Y.; Yang, X.; Hajdinjak, I. C.; Popovic, L. C., 2020, *MNRAS*, 494, 4069  
 Kormendy, J.; Fisher, D. B.; Cornell, M. E.; Bender, R., 2009, *ApJS*, 182, 216  
 Kushwaha, P.; Sarkar, A.; Gupta, A. C.; Tripathi, A.; Wiita, P. J., 2020, *MNRAS*, 499, 653  
 Kharb, P.; Lal, D. V.; Merritt, D., 2017, *NatAs*, 1, 727  
 Kaspi, S.; Smith, P. S.; Netzer, H.; Maoz, D.; Jannuzi, B. T.; Giveon, U., 2000, *ApJ*, 533, 631  
 Kellermann, K. I.; Sramek, R.; Schmidt, M.; Shaffer, D. B.; Green, R., 1989, *AJ*, 98, 1195  
 Kell B. C.; Bechtold J.; Siemiginowska A., 2009, *API*, 698, 895  
 Kozłowski S. et al., 2010, *API*, 708, 927  
 Li, X.; Cai, Y.; Yang, H.; Luo, Y.; Yan, Y.; He, J.; Wang, L., 2021, *MNRAS*, 506, 2540  
 Lacey, C.; Cole, S., 1994, *MNRAS*, 271, 676  
 Lin, L.; Koo, D. C.; Willmer, C. N. A.; et al., 2004, *ApJL*, 617, 9  
 Lokas, E. L., 2023, *A&A*, 673, A131  
 Lauer, T. R.; Boroson, T. A., 2009, *ApJ*, 703, 930  
 Liu, T. T.; Gezari, S.; Heinis, S.; et al., 2015, *ApJL*, 803, L16  
 Liu, X.; Shen, Y.; Bian, F.; Loeb, A.; Tremaine, S., 2014, *ApJ*, 789, 140  
 Liao, W. T.; Chen, Y. C.; Liu, X.; et al., 2021, *MNRAS*, 500, 4025  
 Li, Y. R.; Wang, J. M.; He, Z. Q.; et al., 2016, *ApJ*, 822, 4  
 Lomb, N. R., 1976, *Ap&SS* 39 447  
 Mahabal, A. A.; Djorgovski, S. G.; Drake, A. J.; et al., 2011, *BASI*, 39, 387  
 Menou, K.; Haiman, Z.; Narayanan, V. K., 2001, *ApJ*, 558, 535  
 Merritt, D., 2006, *ApJ*, 648, 976  
 Martin, G.; Jackson, R. A.; Kaviraj, S.; et al., 2021, *MNRAS*, 500, 4937  
 Mayer, L.; Kazantzidis, S.; Escala, A.; Callegari, S., 2010, *Natur*, 466, 1082  
 Mannerkoski, M.; Johansson, P. H.; Rantala, A.; Naab, T.; Liao, S.; Rawlings, A., 2022, *ApJ*, 929, 167  
 Merritt, D.; Milosavljevic, M., 2005, *Living Reviews in Relativity*, 8, 8  
 Marscher, A. P.; Gear, W. K., 1985, *ApJ*, 298, 114  
 Morgan, C. W.; Kochanek, C. S.; Morgan, N. D.; Falco, E. E., 2010, *ApJ*, 712, 1129  
 MacLeod C. L., et al., 2010, *API*, 721, 1014  
 Netzer, H., 2020, *MNRAS*, 494, 1611  
 O'Neill, S.; Kiehlmann, S.; Readhead, A. C. S.; et al., 2022, *ApJL*, 926, L35  
 Pihajoki, P.; Valtonen, M.; Ciprini, S., 2013, *MNRAS*, 434, 3122  
 Peterson, B. M.; Ferrarese, L.; Gilbert, K. M.; et al., 2004, *ApJ*, 613, 682  
 Rodriguez, G. V.; Pillepich, A.; Sales, L. V.; et al., 2016, *MNRAS*, 458, 2371  
 Rodriguez, G. V.; Sales, L. V.; Genel, S.; et al., 2017, *MNRAS*, 467, 3083  
 Rodriguez, C.; Taylor, G. B.; Zavala, R. T.; Peck, A. B.; Pollack, L. K.; Romani, R. W., 2006, *ApJ*, 646, 49  
 Runnoe, J. C.; Eracleous, M.; Mathes, G.; et al., 2015, *ApJS*, 221, 7  
 Silk, J.; Rees, M. J., 1998, *A&A*, 331, L1  
 Satyapal, S.; Ellison, S. L.; McAlpine, W.; Hickox, R. C.; Patton, D. R.; Mendel, J. T., 2014, *MNRAS*, 441, 1297  
 Shields, G. A.; Smith, K. L.; Salvander, S.; Strickler, R.; Dutton, A. A.; Marshall, P. J., 2009, *ApJ*, 707, 936  
 Shen, Y.; Liu, X.; Loeb, A.; Tremaine, S., 2013, *ApJ*, 775, 49  
 Shu, X.; Zhang, W.; Li, S.; et al., 2020, *NatCo*, 11 5876  
 Stella, L.; Vietri, M., 1998, *ApJL*, 491, L59  
 Stella, L.; Vietri, M.; Morsink, S. M., 1999, *ApJL*, 524, L63  
 Songsheng, Y. Y.; Xiao, M.; Wang, J. M.; Ho, L. C., 2020, *ApJS*, 247, 3  
 Sesana, A.; Haiman, Z.; Kocsis, B.; Kelley, L. Z., 2018, *ApJ*, 856, 42  
 Serafinelli, R.; Severgnini, P.; Braito, V.; et al., 2020, *ApJ*, 902, 10  
 Scargle J. D., 1982 *ApJ* 263 835  
 Springford, A.; Eadie, G. M.; Thomson, D. J., 2020, *AJ*, 159, 205  
 Sarkar, A.; Gupta, A. C.; Chitnis, V. R., et al., 2021, *MNRAS*, 501, 50

- Tsalmantza, P.; Decarli, R.; Dotti, M.; Hogg, D. W., 2011, *ApJ*, 738, 20  
Tsang, D.; Lai, D., 2009, *MNRAS*, 396, 589  
Vaughan, S.; Uttley, P.; Markowitz, A. G.; et al., 2016, *MNRAS*, 461, 3145  
Vietri, M.; Stella, L. G., 1998, *ApJ*, 503, 350  
VanderPlas, J. T., 2018, *ApJS*, 236, 16  
Vestergaard, M.; Peterson, B. M. 2006, *ApJ*, 641, 689  
Wang, L. L.; Greene, J. E.; Ju, W. H.; Rafikov, R. R.; Ruan, J. J.; Schneider, D. P., 2017, *ApJ*, 834, 129  
Wandel, A.; Peterson, B. M.; Malkan, M. A., 1999, *ApJ*, 526, 579  
Yoon, Y.; Park, C.; Chung, H.; Lane, R. R., 2022, *ApJ*, 925, 168  
Yang, C.; Ge J.; Lu, Y., 2019, *SCPMA*, 62, 129511  
Zheng, Z. Y.; Butler, N. R.; Shen, Y.; Jiang, L. H.; Wang, J. X.; Chen, X.; Cuadra, J., 2016, *ApJ*, 827, 56  
Zechmeister, M.; Kurster, M., 2009, *A&A*, 496, 577  
Zhang X. G., 2023a, *MNRAS*, 525, 335.  
Zhang X. G., 2022a, *MNRAS*, 512, 1003  
Zhang X. G., 2023b, *MNRAS*, 526, 1588.  
Zhang X. G., 2022b, *MNRAS*, 516, 3650.  
Zhang X. G., 2025a, *ApJ* in press, arXiv:2412.15506  
Zhang X. G., 2025b, *ApJ* in press, arXiv:2503.10050  
Zu Y.; Kochanek C. S.; Kozłowski S.; Udalski A., 2013, *APJ*, 765, 106